JACS
JOURNAL OF THE AMERICAN CHEMICAL SOCIETY
Article
Cite This: J. Am. Chem. Soc. 2019, 141, 4034−4042
pubs.acs.org/JACS

Elucidation of HEPES Affinity to and Structure on Gold Nanostars

Wenjing Xi and Amanda J. Haes*

Department of Chemistry, University of Iowa, Iowa City, Iowa 52242, United States

Supporting Information

ABSTRACT: The zwitterion, *N*-2-hydroxyethylpiperazine-*N*′-2-ethanesulfonic acid (HEPES), facilitates the formation and stability of gold nanostars; however, little is known about how this molecule interacts with the metal postsynthesis. Herein, restructuring of gold nanostar morphology is induced upon acidification, an effect that depends on both pH and acid composition as well as on the protonation state of HEPES. Changes in molecular protonation are measured using zeta potential and modeled using DFT. The surface-sensitive technique, surface-enhanced Raman scattering (SERS), reveals that pH variations induce reversible activation of the amine and sulfonate groups in HEPES and that electron redistribution weakens its affinity to the metal thus promoting the adsorption and SERS detection of benzene. By selecting a molecule that does not induce significant desorption of the stabilizing agent, binding energies of benzene to gold are measured even though only weak London dispersion and $\pi-\pi$ interactions promote adsorption. All in all, this molecular-level insight is expected to facilitate new applications of these nanostructures in ways that have not been possible to date.

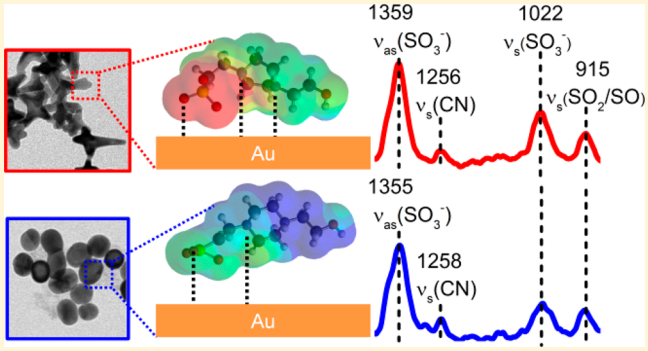

INTRODUCTION

Metallic nanostructures such as gold nanostars (also known as tetrapods, urchins, spiky nanostructures, nanobranches, etc.), nanotriangles,[1] nanobipyramids,[2] and nanocubes[1,3] exhibit large electric fields at their positive and negative curvature sites compared to neutral curvature features and structures,[1] thus facilitating their successful use in sensing[4] and imaging[5] applications. A common approach for synthesizing gold nanostars is a seedless and surfactant-less procedure that uses Good's buffers including HEPES,[6,7] EPPS,[8,9] and MOPS.[10] These reagents act as metal reducing, shape-directing, and stabilizing agents and can result in nanostars with varying sizes and structures[11] that depend on buffer concentration[10] and solution pH.[10] Previous studies primarily focused on manipulating synthetic conditions and tuning plasmon resonances of gold nanostars[12] while applications have been largely limited to self-assembled monolayer functionalized nanostructures.[8,13]

In general, surface chemistry,[14] composition,[14,15] and dimensionality[15] govern nanoparticle properties and function during subsequent use.[16,17] Surface stabilizing agents such as citrate on spheres,[16,18] CTAB on rods,[19−21] and zwitterions such as HEPES or EPPS on stars[22] provide either sufficient electrostatic and/or elastic interfacial energy barriers thus decreasing the likelihood of particle agglomeration and/or aggregation in solution.[23] These reagents, however, also prohibit small molecule adsorption for surface-sensitive techniques such as surface-enhanced Raman scattering (SERS). CTAB, for instance, facilitates the formation of gold nanorods yet does not readily desorb even upon washing.[19]

This is an unsolved problem with many bottom-up synthesized plasmonic nanostructures.[6] As a result, detection of nonthiolated molecules[16,24] using SERS is limited to synthetic modification involving nanoparticle functionalization[25,26] and/or molecular derivatization[25] so that their low binding affinities to the metal can be overcome. This approach often increases the distance between the metal and vibrational chromophore, thus decreasing the observed SERS intensities. Despite this, several studies[27,28] indicate that stabilizing agent disruption and surface cleaning for activation[29] are possible. For instance, Cl^- and Br^- can clean surfaces because of their relatively high (16 kcal/mol) binding affinities for coinage metals.[18,30] While halides can activate a metal for successful SERS detection of molecules such as rhodamine 6G,[18,29] these also increase ionic strength, thus decreasing electrostatic interfacial energies between particles and increasing the probability of nanoparticle aggregation upon collision.[30,31] In addition, these ions can induce etching and/or restructuring via metal−Cl bond formation.[32] While gold nanostars exhibit many desirable features for enhanced spectroscopies because of their inherent morphology, many applications of Good's buffer-reduced gold nanostars are limited to thiolated molecule functionalization.[13] One study revealed that HEPES blocks the metal by forming a bilayer through sulfonate anchoring and hydrogen bonded hydroxyl terminal groups.[22] This surface chemistry structure was stable at HEPES concentrations exceeding 100 mM but underwent collapse upon dilution.[33]

Received: December 10, 2018
Published: February 5, 2019

DOI: 10.1021/jacs.8b13211
J. Am. Chem. Soc. 2019, 141, 4034−4042

Herein, the functional groups in HEPES that bind to gold nanostars upon washing in acidic media are evaluated experimentally using localized surface plasmon resonance (LSPR) spectroscopy, SERS, and zeta potential measurements as well as computationally using DFT calculations. This study reveals that the less acidic nitrogen atom, with a solution-phase pK_a of 7.55 in the piperazine ring, participates in both HEPES stabilization of gold nanostars and reversible surface activation of the metal surface as indicated by SERS detection of benzene, a nonthiolated molecule that interacts with gold through London dispersion forces. This occurs without plasmonic destabilization of the nanostars. This mechanism is confirmed via zeta potential measurements that indicate that the surface pK_a of the aforementioned amine group is depressed by ~4 pH units near gold. This molecular-level insight into how pH impacts the electronic structure of HEPES on gold nanostars is an important step forward for applications that involve these nanoparticles and represents the first example of directly detecting a nonthiolated molecule using these materials while also revealing details regarding surface chemistry on the nanomaterials.

EXPERIMENTAL METHODS

Chemical Reagents. Gold(III) chloride trihydrate ($HAuCl_4 \cdot 3H_2O$), HEPES, and benzene were purchased from Sigma-Aldrich. Sodium hydroxide (NaOH), nitric acid (HNO_3), and ethanol were purchased from Fisher Scientific. Ultrapure water (18.2 MΩ cm^{-1}) was obtained from a Barnstead Nanopure System (Dubuque, IA) and used throughout this study. All glassware was cleaned in a 3:1 HCl/HNO_3 solution and rinsed with water before drying in the oven.

Gold Nanostar Synthesis and Characterization. Gold nanostars were synthesized according to a slightly modified literature protocol.[34] Briefly, the pH of a 40 mM HEPES stock solution was adjusted to 7.48 (±0.01) using 1 M NaOH. Next, 200 μL of a 20 mM $AuCl_4$ aqueous solution was added to 20 mL of the HEPES stock solution and gently agitated for 10 s to ensure homogeneous mixing. The solution was placed in the dark at 21 °C for 1 h to promote nanostar growth. Gold nanostar solutions were centrifuged (30 min, 2400 × *g*), redispersed in 20 mM and then 10 mM HEPES, and stored at 4 °C until use. The linear refractive index sensitivity of the gold nanostars was determined by systematically varying the bulk refractive index of the solution using 0−80% (w/v) sucrose.[8,35]

Gold nanostars were characterized using transmission electron microscopy (TEM, JEOL-1230 equipped with a Gatan CCD camera). Samples were prepared by diluting the nanoparticle solution in ethanol in a 1:1 ratio, which was pipetted onto 400 mesh copper grids coated with a thin film of Formvar and carbon (Ted Pella). TEM images were analyzed (Image Pro Analyzer) to estimate the average dimensionality, where N = the total number of measurements analyzed, and the averages (±standard deviation) of these are reported.

Sample Preparation. Before use, gold nanostars were washed as previously described and resuspended in water to disrupt the HEPES bilayer structure (*vide infra*). Next, ~30 μL of an 18 nM nanostar solution was dispersed in 450 μL of HCl, HNO_3, KCl, KNO_3, or H_2SO_4 solution (final concentration of 1 mM for all except 0.5 mM H_2SO_4) so that the final gold nanostar concentration was 1.1 nM. The nanostar concentration was estimated using a previously determined extinction coefficient (ε = 0.89 nM^{-1} cm^{-1}).[7] To modulate the protonation state of HEPES, ~30 μL of a 24 nM gold nanostar solution was added to 450 μL of water (pH 2.8−7.0, adjusted using HNO_3 unless noted). HNO_3 was used during nanostar pretreatment to minimize gold nanostar restructuring and the resulting plasmonic changes. During pretreatment, LSPR spectra were collected, and a maximum 5 nm blue-shift in the λ_{max} was tolerated so that SERS spectral changes could be positively attributed to local surface chemistry changes and not plasmonic variations. After 10 min of equilibration, 20 μL of a 250 mM benzene stock solution (50% ethanol in water, v/v) was added to the gold nanostar solution so that the final benzene and nanostar concentrations were 10 mM and 1.5 nM, respectively. A similar approach was used in benzene isotherm studies in which gold nanostars with a final concentration of 1.5 nM were pretreated at pH 3 for 10 min before benzene was added (final benzene concentration = 200−7500 μM). Prior to spectroscopic analysis, solutions were vortexed for 10 s. All measurement times were adjusted for lag times in experimental setup.

Normal Raman, SERS, and Extinction Spectroscopies. Normal Raman spectra were collected of 1 M HEPES (pH 7) and neat benzene using a semihomebuilt Raman microscope (ExamineR 785, DeltaNu, Integrated Photonic Solutions 785 nm fiber optically coupled laser). An excitation wavelength (λ_{ex}) of 785 nm, power (P) = 28−58 mW, and integration time (t_{int}) of 5 (Raman) or 25 s (SERS) were used. LSPR spectra were collected using an ultraviolet−visible (UV−vis) spectrometer (i-trometer, B&W Tek). LSPR spectra (integration time = 15 ms, average = 36) were used to track gold nanostar morphology and stability through changes in the extinction maximum wavelength (λ_{max}), which was estimated from zero points of the first derivative. Deconvolution of overlapping vibrational features was performed by calculating second derivative spectra. Vibrational frequencies at significant features (signal-to-noise ratio greater than 3 and full width at half maxima greater than 10 cm^{-1}) were then analyzed using Gaussian functions. All measurements were performed in triplicate unless otherwise noted.

Zeta Potential Measurements. Gold nanostar surface potential was quantified using their electrophoretic mobility collected at 25 °C using a Malvern Zetasizer (Worcestershire, UK). Samples were prepared by incubating 0.4 nM gold nanostars in water (pH from 2.5−7.0) for 10 min as longer incubation times yielded no statistical differences. Zeta potential was calculated using Henry's equation, measured mobilities, and ionic strengths.[36] Error bars represent the standard deviation of three replicate measurements.

DFT Calculations. Electrostatic potential energy was calculated for HEPES in water to determine how electron distribution throughout the molecule changed upon (de)protonation. To do this, energy was minimized using the molecular mechanics model Merck molecular force field (Spartan '16, Version 2.0.7) and then was subsequently followed by density functional theory (DFT) with a basis set of B3LYP/6-31G*. This higher level of theory allowed for accurate modeling of molecular electrostatic potentials.[37,38] Performing calculations in series ensured successful convergence (i.e., energy minimization of optimized geometries) of the calculations. Equilibrium configurations for both deprotonated and protonated HEPES were determined by performing initial energy minimization calculations in Spartan so that structures with the lowest mechanics energies were used as inputs in DFT calculations. Multiple initial configurations were considered by systematically varying atom orientations and distances.[39] Molecular protonation was held constant for a given calculation to simulate experimental conditions. As such, water, which was the experimentally used solvent, was simulated using the SM8 quantum mechanical aqueous continuum solvation model.[40] Electrostatic potential maps were generated in Spartan by first establishing a point charge in electron-rich and electron-poor regions of a molecule. Potential energies with respect to these points were then calculated.[41] Red and blue areas in these maps, as a result, represent relative high and low electron densities, respectively.[39]

RESULTS AND DISCUSSION

Impact of Acid Composition on Gold Nanostar Structure and Plasmonic Properties. Gold nanostars synthesized using bottom-up methods exhibit tunable optical properties that depend on morphology,[42] dielectric environment,[42] and stability.[23] Surface chemistry influences all of these properties. Previously, it was shown that the tips of unfunctionalized gold nanostars underwent blunting over the course of 30 days[43] or upon incubation in some acidic

DOI: 10.1021/jacs.8b13211
J. Am. Chem. Soc. 2019, 141, 4034−4042

media.[44,45] For instance, chloroauric acid[46] and Au^{3+} ions[47] induced etching at regions of high surface energy sites (vertices, edges), thus resulting in spherical nanostructures. In addition, halides serve an important role in the formation of branched nanoparticles as the optical properties and morphology can be tuned by taking advantage of Au−halide chemical affinities.[42] For example, the presence of iodide was shown to inhibit gold nanostar[48] and nanorod[49] growth.

Here, we evaluate how acid composition influences the surface chemistry of gold nanostars through changes in LSPR spectra and morphology. To begin, a representative LSPR spectrum of gold nanostars synthesized using 40 mM HEPES at pH 7.48 is shown in Figure 1A-1. Two plasmonic features

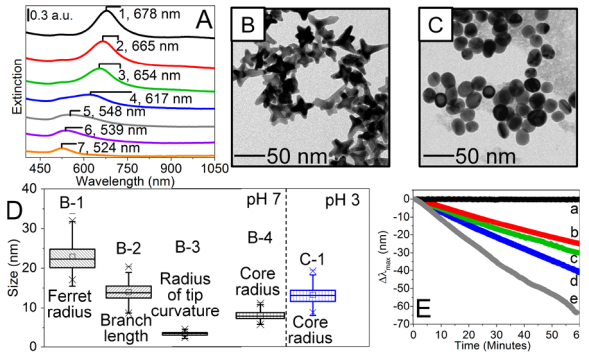

Figure 1. Plasmonic and structural properties of gold nanostars. (A) Representative LSPR spectra of 1.1 nM gold nanostars incubated in 1 mM HNO_3 for (1) 0, (2) 0.5, (3) 1, (4), 2.5, (5) 3.5, (6) 5, and (7) 20 h. Spectra are arbitrarily offset for clarity. TEM images of nanostars incubated in pH (B) 7 and (C) 3 aqueous solutions for 24 h. (D) Evaluation of nanoparticle dimensions at pH 7 include the (B-1) ferret radius (22.9 ± 3.6 nm, N = 105), (B-2) branch length (14.0 ± 2.5 nm, N = 51), (B-3) radius of curvature of the tips (3.43 ± 0.44 nm, N = 148), and (B-4) core radius (8.1 ± 1.1 nm, N = 102), and at pH 3 after 24 h (C-1) average radius (13.2 ± 2.3 nm, N = 173) where N = number of measurements. (E) Evaluation of $\Delta\lambda_{max}$ for nanostars incubated in (a) 1 mM KNO_3, (b) 1 mM KCl, (c) 1 mM HNO_3, (d) 0.5 mM H_2SO_4, and (e) 1 mM HCl as a function of time. $\Delta\lambda_{max}$ represents a change from t_0.

that are centered at 518 and 678 nm represent hybridized resonances associated with the nanostar core and branches,[11] respectively. TEM images (Figure 1B) confirm a morphology that is consistent with these assignments. Namely, the (Figure 1D,B-1) tip-to-tip (ferret) nanostar radius (22.9 ± 3.6 nm, N = 105), (Figure 1D,B-2) branch length (14.0 ± 2.5 nm, N = 51), and (Figure 1D,B-3) radius of curvature of the tips (3.43 ± 0.44 nm, N = 148) (Figure 1D) are observed. Upon incubation in a pH 3 solution prepared using HNO_3, the low energy feature blue-shifts and decreases in magnitude while the other feature red-shifts slightly and increases in magnitude as shown in Figure 1A-2−7. After 20+ hours, only one spectral feature centered at 524 nm is observed, which indicates the formation of spherical nanostructures. This is confirmed using TEM as shown in Figure 1C. Of note, the average core radius of the original nanostars increases from (B-4) 8.1 ± 1.1 nm to (C-1) 13.2 ± 2.3 nm after acid treatment (Figure 1D). This suggests that HNO_3 induces metal ion migration similar to previously reported halide-induced etching.[32] Because no halides or apparent etching reagent is present, we hypothesize that nanostar restructuring likely arises from proton-induced disruption of the stabilizing agent HEPES.

To evaluate this behavior, time-dependent LSPR spectra of 1.1 nM gold nanostars suspended in water are collected for 1 h after incubation in 1 mM KNO_3, 1 mM KCl, 1 mM HNO_3, 0.5 mM H_2SO_4, or 1 mM HCl (pH = 3). These results are summarized in Figure 1E-a,E-b,E-c,E-d,E-e, respectively. In the presence of the acids, the λ_{max} values associated with nanostar branches blue-shift steadily by 28 (±2), 35 (±7), and 67 (±8) nm for HNO_3, H_2SO_4, and HCl, respectively, over the course of an hour. These changes are consistent with gold nanostar restructuring at rates of 0.506 (±0.002), 0.685 (±0.002), and 1.068 (±0.006) nm/min for the same acids.

Anion composition is clearly important in these measurements as revealed through control measurements performed using 1 mM KCl and KNO_3. Similar to previous studies,[32] the halide-containing salt yields a 26 (±2) nm blue-shift in λ_{max} and a restructuring rate of 0.425 (±0.001) nm/min. In contrast, no significant change in λ_{max} is observed for gold nanostars incubated in 1 mM KNO_3 (Figure 1E-a). Furthermore, HCl induces a 67 nm blue-shift in λ_{max} while only a 26 nm blue-shift is observed with KCl, and gold nanostar restructuring occurs ∼2.5 times more quickly in the acid vs halide control. This suggests that both the proton and halide influence particle restructuring. This result differs from the nitrate studies as HNO_3 causes the λ_{max} to blue-shift ∼28 nm while no change was detected in the presence of KNO_3.

These results suggest two things. First, this confirms that restructuring depends on the presence of protons in solution. This behavior is consistent with the acid-induced dissolution of ∼6 nm diameter gold nanospheres.[50] Second, the magnitude and restructuring rate of gold nanostars is likely related to the affinity of the anion to gold. Previously, Cl^- was shown to chemisorb to gold (binding affinity ∼16 kcal/mol)[30] while nitrate and sulfate exhibited a negligible affinity to gold.[29] This suggests a multistep nanostar restructuring process in which acidification leads to a change in HEPES charge, which subsequently allows anions to interact with the metal surface. Consequently, the affinity between neighboring gold atoms weakens, thus promoting their migration and gold nanostar restructuring as shown in Figure 1C. SERS spectra suggest that Cl^- displaces HEPES (data not shown). These TEM and parallel LSPR spectral changes indicate significant nanostar restructuring, and thus HNO_3, which influences morphology the least and exhibited the most reproducible structure−optical property relationship was, as a result, chosen for all subsequent acidification adjustments.

Evaluation of HEPES Interactions to Gold Nanostars. We hypothesize that acidification initially induces gold nanostar restructuring through HEPES protonation, which depends on the surface pK_a of its various functional groups. HEPES, a zwitterion with an isoelectric point of 5.0, contains sulfonate and hydroxide groups that are deprotonated and protonated, respectively, when pH = 1−14.[51] As a result, pH fluctuations from 1 to 14 likely impact the protonation state of either one or both amines in the piperazine ring as shown in Figure 2A. Previously published pK_a values of these two tertiary amines in the piperazine ring are ∼3 and 7.55 for N_1 and N_2, respectively, when the molecule is fully solvated.[51] Upon deprotonation, these form weak covalent bonds to gold via their lone pair electrons[16,52] as shown in Figure 2B.

Surface pK_a values of these nitrogen-containing functional groups are estimated using an established method for thiols[53] where the surface pK_a decreased by ∼10 pH units upon adsorption to gold, and the magnitude of the depression was

DOI: 10.1021/jacs.8b13211
J. Am. Chem. Soc. 2019, 141, 4034−4042

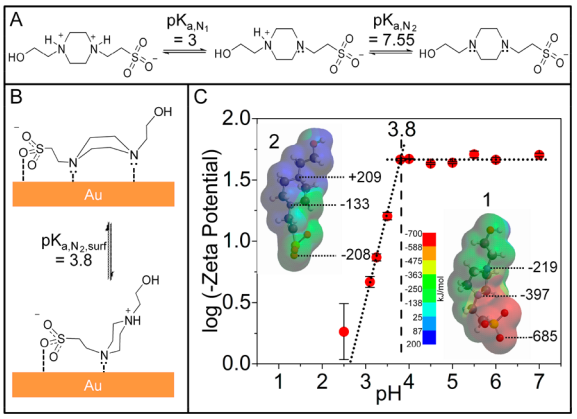

Figure 2. Mechanism of HEPES deprotonation (A) in aqueous solution and (B) on gold nanostructures. (C) Evaluation of 0.4 nM gold nanostar surface potential as a function of pH. The estimated surface p$K_{a,2}$ for N_2 is 3.8 (±0.2). Error bars represent the standard deviation of three replicate measurements. The error in pK_a is estimated from uncertainty in linear analysis. Insets show DFT-optimized geometries and electrostatic potential maps of HEPES when the N_2 amine is (1) deprotonated and (2) protonated.

proportional to the Gibbs free energy (ΔG°) between the functional group and the metal as follows:[53]

$$pK_{a,surf} - pK_{a,soln} = \frac{\Delta G^\circ}{2.303RT} \quad (1)$$

where p$K_{a,surf}$ and p$K_{a,soln}$ are the surface and solution pK_a of the functional groups, respectively, T is temperature, and R is the gas constant.

Using eq 1 and assuming a previously reported Au−N bond strength of 6 kcal/mol,[54,55] a pK_a depression of 4.4 is expected. To experimentally quantify the pK_a of HEPES on gold, the zeta potentials of gold nanostars from pH 2.5 to 7 are evaluated (Figure 2C). Zeta potential is highly negative (−50 mV) in solutions with a pH greater than ~4. Further acidification leads to less negative surface potentials indicating that the amine (N_2) is undergoing protonation. The surface pK_a is easily quantified by taking the log of these values.[56] The inflection point indicates a single surface pK_a, which is estimated at 3.8 (±0.2) as well as a N−Au free energy of adsorption of 5.1 (±0.3) kcal/mol. This result is reasonable for sterically hindered tertiary amines such as HEPES.[57] Assuming the surface pK_a of N_1 decreases by the same magnitude, its surface pK_a should be less than 0. Thus, N_1 is expected to be deprotonated and bonded to gold throughout the pH range here.

All in all, this suggests that solution pH and surface affinity of HEPES to gold influence the electron distribution in the molecule. As a result, the ion/dipole-induced dipole interactions between these species are weakened, thereby leading to reactive conditions that promote gold nanostar restructuring. To provide a semiquantitative comparison of electron distribution changes, electrostatic potential maps are generated for protonated and deprotonated HEPES (insets in Figure 2C). When pH is greater than the pK_a of N_2, electrons are largely localized in the sulfonate group as well as in the piperazine ring but to a lesser extent. Upon acidification and N_2 protonation, the electrostatic potential map changes significantly. These calculated results represent relative electron densities in the molecules with respect to the most positive and negative points in a molecule. As such, negative values (red regions) represent electron-rich regions with respect to the most positive molecular region, and positive values (blue regions) depict electron-poor regions with respect to the most negative molecular region. When HEPES is protonated, the potential energy associated with N_2 becomes positive (−219 to 209 kJ/mol), thus indicating energetically unfavorable interactions to gold. In addition, gold and N_1 or sulfonate interactions weaken from −397 to −133 kJ/mol or from −685 to −208 kJ/mol, respectively, suggesting significant weakening of the HEPES affinity to gold. Because interactions between these functional groups and gold are most likely ion/dipole-induced dipole and these molecular interactions are heavily influenced by electron density,[58] we postulate weakened affinity between the stabilizing agent and metal. It is important, however, to clarify that only the sign and relative change in these values reveal meaningful information.[58] Thus, HEPES likely binds to gold via both the sulfonate and amine groups, and its overall affinity to gold weakens upon N_2 protonation.

These functional group interactions between gold and HEPES are confirmed using SERS. To do this, gold nanostars are rinsed with water to minimize the quantity of HEPES in solution as it interferes with SERS measurements as previously reported.[10] This is likely because HEPES assembles on gold nanostars in a bilayer structure when the HEPES concentration ranges from 10 to 2000 mM.[33] The hydrogen bonding network between hydroxyl groups can be disrupted upon lowering this concentration. As shown in Figure 3A, the LSPR spectra of 1.1

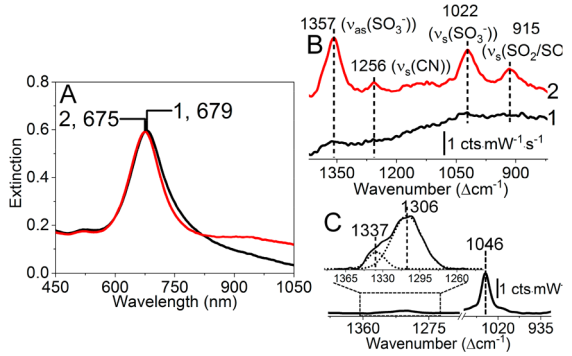

Figure 3. Representative (A) LSPR and (B) SERS spectra for (1) 1.1 nM Au nanostars in 10 mM HEPES (1) before ($\lambda_{max,1}$ = 679 nm) and (2) after washing with water ($\lambda_{max,2}$ = 675 nm). (C) A normal Raman spectrum of 1 M HEPES is shown. The scale of the inset is magnified 30×. Raman collection parameters: λ_{ex} = 785 nm, t_{int} = 25 s, P = 28 mW, average = 3.

nM gold nanostars change only slightly upon decreasing the HEPES concentration in solution. First, the λ_{max} blue-shifts 4 nm upon decreasing the HEPES concentration, which indicates that the local refractive index has decreased by 0.018 RIU (see Figure S1 where a 284 nm/RIU sensitivity is determined and used to quantify RI variations). Second, the LSPR magnitude from 800 to 1050 nm increases slightly, a response consistent with electromagnetic coupling between branches on a given nanostructure or between nanostars.[23,59] SERS analysis confirms this mechanism as HEPES is observed upon washing the nanostars with water and bilayer disruption (Figure 3B-2) whereas HEPES is not observed at higher concentrations (Figure 3B-1). A spectrum of 1 M HEPES using normal Raman is shown for comparison and band assignments (Figure 3C).

DOI: 10.1021/jacs.8b13211
J. Am. Chem. Soc. 2019, 141, 4034−4042

Implications of HEPES disruption and/or removal are evaluated as a function of pH. To do this, 1.5 nM gold nanostar solutions are pretreated using a pH 2.8−7 solution for 10 min before collecting SERS data. Figure 4A,B shows

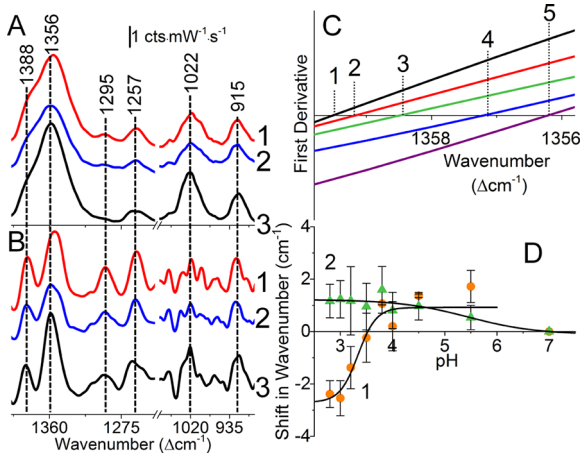

Figure 4. Representative (A) SERS, (B) inverse second derivative, and (C) first derivative spectra of residual HEPES on 1.1 nM gold nanostars in aqueous solution. Panels A and B: pH = (1) 3.0, (2) 3.5, and (3) 7. Panel C: pH = (1) 4.5, (2) 3.8, (3) 3.5, (4) 3.2, (5) 3.0. Vibrational band assignments are found in Table 1. (D) pH-dependent vibrational frequency shifts relative to solution for the (1) SO_3^- asymmetric and (2) C−N stretches are shown. Raman collection parameters: λ_{ex} = 785 nm, t_{int} = 25 s, P = 28 mW, average = 3.

representative SERS and second derivative spectra of HEPES at pH (1) 3.0, (2) 3.5, and (3) 7. The second derivative spectra are inverted to mimic spectral data to facilitate small spectral feature identification vs the broad background continuum, which is induced from metal−molecule coupling, image dipole, and nanomaterial morphological changes.[60]

Several spectral features (Table 1) consistent with changes in the previously described electron distribution in HEPES are

Table 1. Normal Raman and SERS Vibrational Mode Assignments[a]

mode	Raman (lit.), cm^{-1}	Raman (this work), cm^{-1}	SERS (lit.), cm^{-1}	SERS (this work) cm^{-1}
$\delta(CH_2)$[61]	1475−1450	ND	ND	1388
$\tau(CH_2)$[67]	1310−1260	1337, 1306 (w)	ND	1295
$\nu_{as}(SO_3)$[68−70]	1380	ND	ND	1359−1356
$\nu_s(CN)$[61]	1280−1180	ND	ND	1258−1256
$\nu_s(SO_3)$[70,71]	1053	1046 (s)	ND	1022
$\nu_s(SO_2)$,[66] $\nu_s(SO)$[72]	958	ND	917	915

[a]Abbreviations include scissor (δ), twist (τ), asym stretch (ν_{as}), sym stretch (ν_s), weak (w), strong (s), not detected (nd)

noted. First, the most intense vibrational features are associated with the sulfonate (asymmetric stretch of SO_3^- (1359−1356 cm^{-1})) and amine (C−N stretching mode (1258−1256 cm^{-1})) groups.[61,62] Of note, these modes are not observed in normal Raman spectra as they are forbidden modes unless symmetry is broken, for instance, through gold−molecule interactions.[63] Second, the most intense feature in the normal Raman data for HEPES (Figure 3C) is associated with the SO_3^- symmetric stretch (1046 cm^{-1}).[64−66] This band red-shifts 26 cm^{-1} to 1020 cm^{-1} in SERS vs normal Raman, which indicates that the sulfonate group participates in binding to the gold surface likely from electron transfer from the molecule to the metal thereby weakening the S−O bonds.[63] Our present studies, which are measured at residual HEPES levels, suggest cooperative pH dependencies on the affinity of HEPES to gold. This is further supported by evaluating pH-dependent vibrational frequencies in the first derivative SERS spectra (Figure 4C) compared to calculated electrostatic potentials. For instance, both the asymmetric SO_3^- stretch and the C−N stretching frequencies are small but easily observed from their first derivative. Zero point crossing values reveal relevant vibrational frequencies and are reported as a function of pH in Figure 4D for both modes. As pH decreases below 4, the C−N stretching frequency blue-shifts from 1256.4 (±0.7) to 1257.6 (±0.1) cm^{-1}. While small, this suggests a slight weakening in binding affinity between N and Au. In contrast, the asymmetric stretching frequency associated with sulfonate red-shifts from 1359.1 (±0.3) to 1355.8 (±0.3) cm^{-1}, a response consistent with electron density decreasing in this functional group and subsequent weakening affinity to gold as predicted from DFT. It should be noted that the SERS intensities of these modes are independent of solution pH thus indicating that HEPES does not desorb.

Implications of HEPES Disruption on the SERS Detection of Benzene. If acidification induces a weakening of HEPES affinity to gold, SERS activity of weakly binding molecules such as benzene might be observable. Benzene was chosen as its binding affinity to gold is governed by relatively weak London dispersion forces[73] and, thus, should not exceed that of the stabilizing agent.[74] To study this, gold nanostars are initially pretreated with HNO_3. These solutions are equilibrated for 10 min to allow for electron redistribution in HEPES yet minimize impacts of gold atom migration before benzene is added. Because gold nanostar aggregation and restructuring dominate spectral changes in solution when the pH is below 3, these conditions were not further considered.

As shown in SERS analysis (Figure 5A), 10 mM benzene is successfully detected with the largest signals detected from the most acidic solution. Only two vibrational features are observed including the asymmetric stretch associated with the sulfonate group of HEPES (1360 cm^{-1}) and the ring breathing mode,[75] associated with benzene (964 cm^{-1} with a less intense shoulder at 979 cm^{-1}). Previously, the shoulder was attributed to benzene interacting with another benzene via $\pi-\pi$ interactions.[76] Interestingly, this shoulder is largest at pH 3 as shown in the second derivative SERS spectra where there is benzene adsorption to gold and, thus, $\pi-\pi$ interactions are most energetically favorable. Second, the intensity of the ring breathing mode at 964 cm^{-1} for benzene increases by almost an order of magnitude when pH decreases from above the surface pK_a of HEPES to 3 (Figure 5A). As the benzene signal increases, the HEPES vibrational mode decreases and becomes indistinguishable from noise at the most acidic pH.

This result indicates that HEPES is partially displaced by benzene and undergoes reorientation upon benzene adsorption,[8] and/or the chemical enhancement[77] associated with the sulfonate bands from HEPES decreases upon acidification. We postulate that partial desorption of and changes in electron distribution in HEPES lead to this observation. To evaluate if the pH-dependent binding affinity of HEPES is reversible, gold

DOI: 10.1021/jacs.8b13211
J. Am. Chem. Soc. 2019, 141, 4034−4042

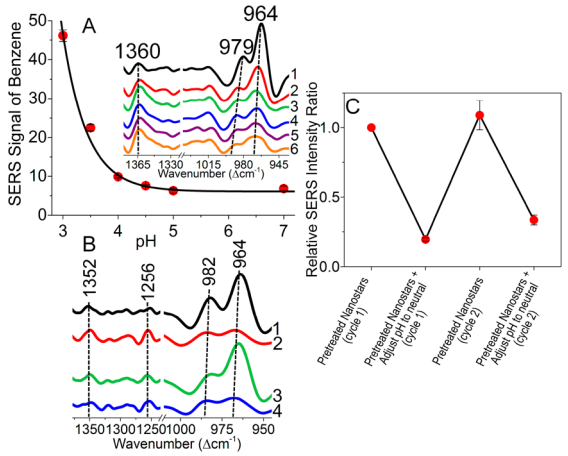

Figure 5. SERS analysis (inset-inverse second derivative) of (A) 10 mM benzene incubated with 1.5 nM nanostars for 30 min after an initial 10 min pretreatment in water with a pH of (1) 3, (2) 3.5, (3) 4.0, (4) 4.5, (5) 5.5, and (6) 7.0. (B) SERS spectra (inverse second derivative) of 5 mM benzene after (1) pretreatment in pH 3 water for 10 min, (2) step 1 + neutralization for 5 min, (3) steps 1 + 2 + 1, and (4) steps 1 + 2 + 1 + 2. (C) Relative integrated areas of the ring breathing mode for benzene (1006−936 cm^{-1}) to the asymmetric sulfonate stretch are shown. This ratio is reported relative to the first data point (pH 3 in cycle 1). Vibrational band assignments: 1360 (HEPES, SO_3 asymmetric stretch), 964, and 979 cm^{-1} (benzene, ring breathing). Raman parameters: λ_{ex} = 785 nm, t_{int} = 25 s, P = 28−58 mW, average = 3.

nanostars are pretreated as previously described. Next, the pH of this solution is repeatedly cycled between 7 and/or 3 before 5 mM benzene is added. After 20 min, SERS spectra are collected to evaluate surface activity (Figure 5B,C) and reveal that both the HEPES and benzene signals depend on pH and are reversible. Representative second derivative SERS spectra show that the two vibrational features associated with benzene are smaller upon incubation at pH 7 (Figure 5B-2,B-4 and Figure S2A) vs pH 3 (Figure 5B-1,B-3 and Figure S2A). The signals collected at pH 3 are approximately constant between the first and second pH cycling process. It is interesting to note that the ring breathing mode for benzene adsorbed to gold blue-shifts from 964 to 967 cm^{-1} while the loosely bound feature varies from 982 to 985 cm^{-1} when pH increases from 3 to 7. This 3 cm^{-1} blue-shift for both bands indicates less energetically favorable benzene adsorption conditions when N_2 in HEPES is deprotonated (pH 7) vs protonated (pH 3).

The HEPES features associated with C−N stretching (1256 cm^{-1}) (Figure S2B-1) and sulfonate asymmetric stretching (1352 cm^{-1}) (Figure S2B-3) exhibit opposite behavior relative to that of benzene. That is, the signals are large at pH 7 and small at pH 3. In addition, changes in these signals are reversible and depend on benzene addition and not pH alone (Figure S2B). This is clearly shown in Figure S2B-3,B-4 where the SERS signals associated with the asymmetric sulfonate stretch at 1352 cm^{-1} are largely independent of pH cycling in the absence of benzene. After 2 cycles, this band reduces in intensity but does not completely disappear indicating that HEPES remains on the gold surface. Further pH cycling leads to electromagnetic coupling between nanostars so this was not further considered. The SERS signal variations support the hypothesis that the binding affinity of HEPES depends on pH and is largely reversible. We estimate that the binding affinity of HEPES decreases by at least 5.1 kcal/mol when N_2 becomes protonated (i.e., when pH ≤ 3.8). This would lead to small HEPES signals when benzene features are large because of energetically favorable binding conditions.

To further investigate the implications of surface activation at pH 3, the binding affinity of benzene to 1.5 nM gold nanostars is evaluated. Representative time-dependent SERS spectra of 1500 μM benzene (Figure S3A) reveal spectral features associated with the ring breathing mode of benzene (964 cm^{-1}) and weakly bound benzene from $\pi-\pi$ interactions (979 cm^{-1}). Results using 200−7500 μM benzene are summarized in Figure S3B and show that the total signal associated with benzene reaches equilibrium within 30 min. To compare signal variations at equilibrium, spectra collected at 30 min are evaluated (Figure 6A). Spectral features from both

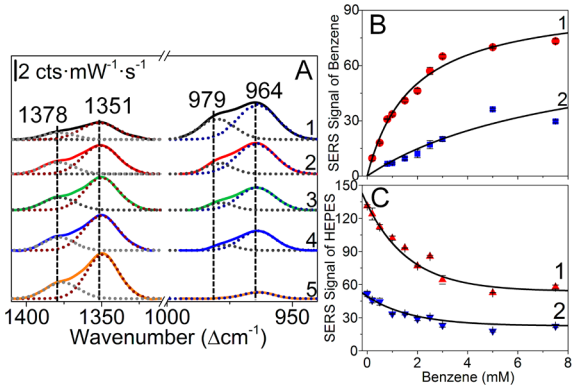

Figure 6. Benzene adsorption to 1.1 nM gold nanostars. (A) Representative SERS spectra of (1) 5, (2) 2.5, (3) 1.5, (4) 1.0, and (5) 0.2 mM benzene incubated with nanostars for 30 min after an initial 10 min pretreatment. Trends in signals for (B) benzene features centered at (1) 964 (±0.5) cm^{-1} and (2) 979 (±1.2) cm^{-1} and (C) HEPES at (1) 1351 (±0.8) cm^{-1} and (2) 1378 (±0.9) cm^{-1}. Fits for panels B and C are from eq 2. Raman parameters follow: λ_{ex} = 785 nm, t_{int} = 25 s, P = 28 mW, average = 3.

benzene and HEPES (1378 cm^{-1}, CH_2 scissoring, and 1351 cm^{-1}, SO_3 asymmetric stretching) are observed in all spectra while only the ring breathing mode located at 964 cm^{-1} is observed at the lowest benzene concentration. Signals associated with benzene increase but decrease for HEPES with increasing benzene concentration until steady-state is reached. Closer evaluation of these spectral features is achieved through spectral deconvolution and second derivative analysis,[78] which are summarized in Figure 6B,C for all bands independently. Interestingly, the vibrational features for HEPES (Figure 6C) decrease by ∼50% as benzene concentration increases from 0 to 5 mM. This suggests that approximately half of the HEPES molecules are displaced by the addition of benzene.

The data follow Langmuir-like behavior for both spectral features of benzene as follows:

$$I_{SERS} = I_{SERS}^{max}\left(\frac{K_{eq}C}{1 + K_{eq}C}\right) \quad (2)$$

where I_{SERS} is the band area obtained from spectral deconvolution for a given benzene concentration (C), I_{SERS}^{max} is the maximum signal, and K_{eq} is the equilibrium constant (in mM^{-1}). Estimated K_{eq} values are 0.56 (±0.05) and 0.12 (±0.04) mM^{-1} for the ring breathing mode directly adsorbed to gold (964 cm^{-1}) and for $\pi-\pi$ interacting species (979

DOI: 10.1021/jacs.8b13211
J. Am. Chem. Soc. 2019, 141, 4034−4042

cm^{-1}), respectively. Corresponding Gibbs free energies of adsorption ($\Delta G_{ads} = -RT \ln(K_{eq})$) are −3.69 (±0.06) and −2.80 (±0.20) kcal/mol. We postulate that the binding affinity of HEPES is approximately this same magnitude (of benzene to gold) at pH 3 and increases as the pH increases further.

All in all, these results support that benzene adsorbs to gold with its ring parallel to the interface. While the adsorption free energies are small and of the same magnitude, this is reasonable given that both London dispersion and $\pi-\pi$ interactions exhibit similar energies.[79,80] Because the most intense vibrational mode is associated with London dispersion forces between benzene and gold, the band red-shifts ∼32 cm^{-1} from the normal Raman frequency in solution (996 cm^{-1}) consistent with π orbital overlap between benzene and gold.[75] By comparison, a 17 cm^{-1} red-shift in vibrational mode for benzene interacting via $\pi-\pi$ interactions is relatively weaker, thus leading to slightly less energetically favorable binding interactions.

CONCLUSIONS

HEPES was shown to influence gold nanostar stability and SERS detection of benzene through changes in its pH-dependent electron distribution and, as a result, affinity to the gold surface. While surface stabilizing agents play important roles in bottom-up synthesized nanomaterials, vibrational mode variations are consistent with disruption of the electron distribution in HEPES on the nanostar surface. These effects are likely dependent on the chemical potential of the gold surface and could be relevant when other gold materials are used. Importantly, the binding affinity and structure of HEPES on gold nanostars are largely influenced by solution pH and the surface pK_a depression of its N_2 amine group on gold relative to solution. This impacts the morphology, surface potential, and surface activity of the nanostars as well as their subsequent use in SERS detection of benzene. While morphology changes from gold nanoparticle restructuring are irreversible, all other effects including the binding affinity of HEPES and the detectability of benzene are reversible and attributed to changes in the affinity between gold and both the sulfonate and amine groups in the piperazine ring. Notably, the affinity of HEPES to gold weakens upon acidification leading to slight but incomplete desorption of HEPES. Changes in electron distribution of HEPES were confirmed using DFT, SERS, and LSPR. Upon protonation of one of the amine groups, benzene adsorbed to the gold surface through London dispersion forces as well as to other benzene molecules via $\pi-\pi$ interactions. All in all, this work suggests that surface-enhanced spectroscopy analysis of small molecule stabilizing agents depends on many factors including electron redistribution in stabilizing agents and surface availability. Importantly, the pH-dependent behavior described in this work can likely be extended to gold nanostars prepared using other Good's buffers such as MOPS and EPPS. Nearly identical trends are likely for EPPS versus HEPES given the similarity of functional groups and pK_a values. While it has a similar pK_a, MOPS contains a morpholine ring and sulfonate functional group. As such, surface stabilization and structure preservation arise from unique intermolecular interactions. Disruption of these interactions is possible but can also induce morphology changes. By doing so, the importance of pH on stabilizing agent functional group affinity was exploited, an impact that could be extended to other nanostructures as well as to other analytes that have a weak affinity for gold and/or other plasmonic materials.

ASSOCIATED CONTENT

Supporting Information

The Supporting Information is available free of charge on the ACS Publications website at DOI: 10.1021/jacs.8b13211.

Refractive index sensitivity of gold nanostars, reversibility of hepes adsorption to gold, and time-dependent adsorption of benzene to gold nanostars (PDF)

AUTHOR INFORMATION

Corresponding Author

*amanda-haes@uiowa.edu

ORCID

Wenjing Xi: 0000-0003-1284-2056

Amanda J. Haes: 0000-0001-7232-6825

Notes

The authors declare no competing financial interest.

ACKNOWLEDGMENTS

We thank Hoa T. Phan for collecting TEM and Sajeewani Kumarage for preparing gold nanostars. Research reported in this publication was supported by the National Science Foundation (CHE-1707859).

REFERENCES

(1) Reguera, J.; Langer, J.; de Aberasturi, D. J.; Liz-Marzán, L. M. Anisotropic Metal Nanoparticles for Surface Enhanced Raman Scattering. *Chem. Soc. Rev.* **2017**, *46*, 3866−3885.

(2) Chen, H.; Kou, X.; Yang, Z.; Ni, W.; Wang, J. Shape- and Size-Dependent Refractive Index Sensitivity of Gold Nanoparticles. *Langmuir* **2008**, *24*, 5233−5237.

(3) Akselrod, G. M.; Huang, J.; Hoang, T. B.; Bowen, P. T.; Su, L.; Smith, D. R.; Mikkelsen, M. H. Large-Area Metasurface Perfect Absorbers from Visible to near-Infrared. *Adv. Mater.* **2015**, *27*, 8028−8034.

(4) Liu, Y.; Yuan, H.; Kersey, F.; Register, J.; Parrott, M.; Vo-Dinh, T. Plasmonic Gold Nanostars for Multi-Modality Sensing and Diagnostics. *Sensors* **2015**, *15*, 3706−3720.

(5) Rodríguez-Lorenzo, L.; Krpetic, Z.; Barbosa, S.; Alvarez-Puebla, R. A.; Liz-Marzán, L. M.; Prior, I. A.; Brust, M. Intracellular Mapping with SERS-Encoded Gold Nanostars. *Integr. Biol.* **2011**, *3*, 922−926.

(6) Webb, J. A.; Erwin, W. R.; Zarick, H. F.; Aufrecht, J.; Manning, H. W.; Lang, M. J.; Pint, C. L.; Bardhan, R. Geometry-Dependent Plasmonic Tunability and Photothermal Characteristics of Multi-branched Gold Nanoantennas. *J. Phys. Chem. C* **2014**, *118*, 3696−3707.

(7) de Puig, H.; Tam, J. O.; Yen, C.-W.; Gehrke, L.; Hamad-Schifferli, K. Extinction Coefficient of Gold Nanostars. *J. Phys. Chem. C* **2015**, *119*, 17408−17415.

(8) Lu, G.; Forbes, T. Z.; Haes, A. J. SERS Detection of Uranyl Using Functionalized Gold Nanostars Promoted by Nanoparticle Shape and Size. *Analyst* **2016**, *141*, 5137−5143.

(9) Cai, J.; et al. Controllable Synthesis of Tetrapod Gold Nanocrystals with Precisely Tunable near-Infrared Plasmon Resonance Towards Highly Efficient Surface Enhanced Raman Spectroscopy Bioimaging. *J. Mater. Chem. B* **2015**, *3*, 7377−7385.

(10) Chandra, K.; Culver, K. S. B.; Werner, S. E.; Lee, R. C.; Odom, T. W. Manipulating the Anisotropic Structure of Gold Nanostars Using Good's Buffers. *Chem. Mater.* **2016**, *28*, 6763−6769.

(11) Hao, F.; Nehl, C. L.; Hafner, J. H.; Nordlander, P. Plasmon Resonances of a Gold Nanostar. *Nano Lett.* **2007**, *7*, 729−732.

(12) Liu, X.-L.; Wang, J.-H.; Liang, S.; Yang, D.-J.; Nan, F.; Ding, S.-J.; Zhou, L.; Hao, Z.-H.; Wang, Q.-Q. Tuning Plasmon Resonance of

DOI: 10.1021/jacs.8b13211
J. Am. Chem. Soc. 2019, 141, 4034−4042

Gold Nanostars for Enhancements of Nonlinear Optical Response and Raman Scattering. *J. Phys. Chem. C* **2014**, *118*, 9659−9664.
(13) Su, Q.; Ma, X.; Dong, J.; Jiang, C.; Qian, W. A Reproducible SERS Substrate Based on Electrostatically Assisted Aptes-Functionalized Surface-Assembly of Gold Nanostars. *ACS Appl. Mater. Interfaces* **2011**, *3*, 1873−1879.
(14) Gatoo, M. A.; Naseem, S.; Arfat, M. Y.; Mahmood Dar, A.; Qasim, K.; Zubair, S. Physicochemical Properties of Nanomaterials: Implication in Associated Toxic Manifestations. *BioMed Res. Int.* **2014**, *2014*, 1.
(15) Ray, P. C. Size and Shape Dependent Second Order Nonlinear Optical Properties of Nanomaterials and Their Application in Biological and Chemical Sensing. *Chem. Rev.* **2010**, *110*, 5332−5365.
(16) Xi, W.; Shrestha, B. K.; Haes, A. J. Promoting Intra- and Intermolecular Interactions in Surface-Enhanced Raman Scattering. *Anal. Chem.* **2018**, *90*, 128−143.
(17) Contreras-Cáceres, R.; Sierra-Martín, B.; Ferna′ndez-Barbero, A. Surface-Enhanced Raman Scattering Sensors Based on Hybrid Nanoparticles. In *Microsensors*; Minon, I., Eds.; InTech: London, 2011.
(18) Hildebrandt, P.; Stockburger, M. Surface-Enhanced Resonance Raman Spectroscopy of Rhodamine 6g Adsorbed on Colloidal Silver. *J. Phys. Chem.* **1984**, *88*, 5935−5944.
(19) Lee, S.; Anderson, L. J.; Payne, C. M.; Hafner, J. H. Structural Transition in the Surfactant Layer That Surrounds Gold Nanorods as Observed by Analytical Surface-Enhanced Raman Spectroscopy. *Langmuir* **2011**, *27*, 14748−14756.
(20) Liu, Y.; Tourbin, M.; Lachaize, S.; Guiraud, P. Silica Nanoparticles Separation from Water: Aggregation by Cetyltrimethylammonium Bromide (CTAB). *Chemosphere* **2013**, *92*, 681−687.
(21) Wang, W.; Gu, B.; Liang, L.; Hamilton, W. A. Adsorption and Structural Arrangement of Cetyltrimethylammonium Cations at the Silica Nanoparticle− Water Interface. *J. Phys. Chem. B* **2004**, *108*, 17477−17483.
(22) Yuan, H.; Fales, A. M.; Khoury, C. G.; Liu, J.; Vo-Dinh, T. Spectral Characterization and Intracellular Detection of Surface-Enhanced Raman Scattering (SERS)-Encoded Plasmonic Gold Nanostars. *J. Raman Spectrosc.* **2013**, *44*, 234−239.
(23) Xi, W.; Phan, H. T.; Haes, A. J. How to Accurately Predict Solution-Phase Gold Nanostar Stability. *Anal. Bioanal. Chem.* **2018**, *410*, 6113−6123.
(24) DeVetter, B. M.; Mukherjee, P.; Murphy, C. J.; Bhargava, R. Measuring Binding Kinetics of Aromatic Thiolated Molecules with Nanoparticles via Surface-Enhanced Raman Spectroscopy. *Nanoscale* **2015**, *7*, 8766−8775.
(25) Sperling, R. A.; Parak, W. J. Surface Modification, Functionalization and Bioconjugation of Colloidal Inorganic Nanoparticles. *Philos. Trans. R. Soc., A* **2010**, *368*, 1333−1383.
(26) Kubackova, J.; Fabriciova, G.; Miskovsky, P.; Jancura, D.; Sanchez-Cortes, S. Sensitive Surface-Enhanced Raman Spectroscopy (SERS) Detection of Organochlorine Pesticides by Alkyl Dithiol-Functionalized Metal Nanoparticles-Induced Plasmonic Hot Spots. *Anal. Chem.* **2015**, *87*, 663−669.
(27) Farquharson, S.; Shende, C.; Sengupta, A.; Huang, H.; Inscore, F. Rapid Detection and Identification of Overdose Drugs in Saliva by Surface-Enhanced Raman Scattering Using Fused Gold Colloids. *Pharmaceutics* **2011**, *3*, 425−439.
(28) El-Zahry, M. R.; Refaat, I. H.; Mohamed, H. A.; Lendl, B. Sequential SERS Determination of Aspirin and Vitamin C Using in Situ Laser-Induced Photochemical Silver Substrate Synthesis in a Moving Flow Cell. *Anal. Bioanal. Chem.* **2016**, *408*, 4733−4741.
(29) Doering, W. E.; Nie, S. Single-Molecule and Single-Nanoparticle SERS: Examining the Roles of Surface Active Sites and Chemical Enhancement. *J. Phys. Chem. B* **2002**, *106*, 311−317.
(30) Zhang, Z.; Li, H.; Zhang, F.; Wu, Y.; Guo, Z.; Zhou, L.; Li, J. Investigation of Halide-Induced Aggregation of Au Nanoparticles into Spongelike Gold. *Langmuir* **2014**, *30*, 2648−2659.
(31) Han, S.; Hong, S.; Li, X. Effects of Cations and Anions as Aggregating Agents on SERS Detection of Cotinine (COT) and Trans-3′-Hydroxycotinine (3HC). *J. Colloid Interface Sci.* **2013**, *410*, 74−80.
(32) Tang, B.; Xu, S.; An, J.; Zhao, B.; Xu, W.; Lombardi, J. R. Kinetic Effects of Halide Ions on the Morphological Evolution of Silver Nanoplates. *Phys. Chem. Chem. Phys.* **2009**, *11*, 10286−10292.
(33) Liu, H.; Xu, Y.; Qin, Y.; Sanderson, W.; Crowley, D.; Turner, C. H.; Bao, Y. Ligand-Directed Formation of Gold Tetrapod Nanostructures. *J. Phys. Chem. C* **2013**, *117*, 17143−17150.
(34) Xie, J.; Lee, J. Y.; Wang, D. I. Seedless, Surfactantless, High-Yield Synthesis of Branched Gold Nanocrystals in Hepes Buffer Solution. *Chem. Mater.* **2007**, *19*, 2823−2830.
(35) Sobral, H.; Peña-Gomar, M. Determination of the Refractive Index of Glucose-Ethanol-Water Mixtures Using Spectroscopic Refractometry near the Critical Angle. *Appl. Opt.* **2015**, *54*, 8453−8458.
(36) Ohshima, H. A Simple Expression for Henry's Function for the Retardation Effect in Electrophoresis of Spherical Colloidal Particles. *J. Colloid Interface Sci.* **1994**, *168*, 269−271.
(37) Drissi, M.; Benhalima, N.; Megrouss, Y.; Rachida, R.; Chouaih, A.; Hamzaoui, F. Theoretical and Experimental Electrostatic Potential around the M-Nitrophenol Molecule. *Molecules* **2015**, *20*, 4042−4054.
(38) Köster, A. M.; Leboeuf, M.; Salahub, D. R. Molecular Electrostatic Potentials from Density Functional Theory. In *Theoretical and Computational Chemistry*; Murray, J. S., Sen, K., Eds.; Elsevier: Amsterdam, 1996.
(39) Hehre, W.; Ohlinger, S. *Spartan Tutorial and User's Guide*; Wavefunction, Inc.: Irvine, CA, 2010.
(40) Bondesson, L.; Mikkelsen, K. V.; Luo, Y.; Garberg, P.; Ågren, H. Hydrogen Bonding Effects on Infrared and Raman Spectra of Drug Molecules. *Spectrochim. Acta, Part A* **2007**, *66*, 213−224.
(41) Politzer, P.; Laurence, P. R.; Jayasuriya, K. Molecular Electrostatic Potentials: An Effective Tool for the Elucidation of Biochemical Phenomena. *Environ. Health Perspect.* **1985**, *61*, 191−202.
(42) De Silva Indrasekara, A. S.; Johnson, S. F.; Odion, R. A.; Vo-Dinh, T. Manipulation of the Geometry and Modulation of the Optical Response of Surfactant-Free Gold Nanostars: A Systematic Bottom-up Synthesis. *ACS Omega* **2018**, *3*, 2202−2210.
(43) Vega, M. M.; Bonifacio, A.; Lughi, V.; Marsi, S.; Carrato, S.; Sergo, V. Long-Term Stability of Surfactant-Free Gold Nanostars. *J. Nanopart. Res.* **2014**, *16*, 2729.
(44) Zhao, L.; Ji, X.; Sun, X.; Li, J.; Yang, W.; Peng, X. Formation and Stability of Gold Nanoflowers by the Seeding Approach: The Effect of Intraparticle Ripening. *J. Phys. Chem. C* **2009**, *113*, 16645−16651.
(45) Hojo, M.; Yamamoto, M.; Okamura, K. Dilute Nitric or Nitrous Acid Solution Containing Halide Ions as Effective Media for Pure Gold Dissolution. *Phys. Chem. Chem. Phys.* **2015**, *17*, 19948−19956.
(46) Lee, Y.-J.; Schade, N. B.; Sun, L.; Fan, J. A.; Bae, D. R.; Mariscal, M. M.; Lee, G.; Capasso, F.; Sacanna, S.; Manoharan, V. N.; Yi, G.-R. Ultrasmooth, Highly Spherical Monocrystalline Gold Particles for Precision Plasmonics. *ACS Nano* **2013**, *7*, 11064−11070.
(47) Yoon, J. H.; Selbach, F.; Langolf, L.; Schlücker, S. Ideal Dimers of Gold Nanospheres for Precision Plasmonics: Synthesis and Characterization at the Single-Particle Level for Identification of Higher Order Modes. *Small* **2018**, *14*, 1702754−1702759.
(48) Kedia, A.; Kumar, P. S. Halide Ion Induced Tuning and Self-Organization of Gold Nanostars. *RSC Adv.* **2014**, *4*, 4782−4790.
(49) Smith, D. K.; Miller, N. R.; Korgel, B. A. Iodide in CTAB Prevents Gold Nanorod Formation. *Langmuir* **2009**, *25*, 9518−9524.
(50) Tripathy, S. K.; Woo, J. Y.; Han, C.-S. Highly Selective Colorimetric Detection of Hydrochloric Acid Using Unlabeled Gold Nanoparticles and an Oxidizing Agent. *Anal. Chem.* **2011**, *83*, 9206−9212.
(51) Al-Ghobashy, M. A. Electrophoretic Behavior of Charge Regulated Zwitter Ionic Buffers in Covalently and Dynamically Coated Fused Silica Capillaries. *Bull. Fac. Pharm.* **2014**, *52*, 71−78.

DOI: 10.1021/jacs.8b13211
J. Am. Chem. Soc. 2019, 141, 4034−4042

(52) Chen, F.; Li, X.; Hihath, J.; Huang, Z.; Tao, N. Effect of Anchoring Groups on Single-Molecule Conductance: Comparative Study of Thiol-, Amine-, and Carboxylic-Acid-Terminated Molecules. *J. Am. Chem. Soc.* **2006**, *128*, 15874−15881.
(53) Ansar, S. M.; Perera, G. S.; Jiang, D.; Holler, R. A.; Zhang, D. Organothiols Self-Assembled onto Gold: Evidence for Deprotonation of the Sulfur-Bound Hydrogen and Charge Transfer from Thiolate. *J. Phys. Chem. C* **2013**, *117*, 8793−8798.
(54) Tarazona-Vasquez, F.; Balbuena, P. B. Complexation of the Lowest Generation Poly(Amidoamine)-NH_2 Dendrimers with Metal Ions, Metal Atoms, and Cu(II) Hydrates: An Ab Initio Study. *J. Phys. Chem. B* **2004**, *108*, 15992−16001.
(55) Di Felice, R.; Selloni, A. Adsorption Modes of Cysteine on Au (111): Thiolate, Amino-Thiolate, Disulfide. *J. Chem. Phys.* **2004**, *120*, 4906−4914.
(56) Charron, G.; Hühn, D.; Perrier, A. l.; Cordier, L.; Pickett, C. J.; Nann, T.; Parak, W. J. On the Use of pH Titration to Quantitatively Characterize Colloidal Nanoparticles. *Langmuir* **2012**, *28*, 15141−15149.
(57) Alder, R. W. Strain Effects on Amine Basicities. *Chem. Rev.* **1989**, *89*, 1215−1223.
(58) Brem, S.; Schlücker, S. Surface-Enhanced Raman Spectroscopy and Density Functional Theory Calculations of a Rationally Designed Rhodamine with Thiol Groups at the Xanthene Ring. *J. Phys. Chem. C* **2017**, *121*, 15310−15317.
(59) Wijenayaka, L. A.; Ivanov, M. R.; Cheatum, C. M.; Haes, A. J. Improved Parametrization for Extended Derjaguin, Landau, Verwey, and Overbeek Predictions of Functionalized Gold Nanosphere Stability. *J. Phys. Chem. C* **2015**, *119*, 10064−10075.
(60) Hugall, J. T.; Baumberg, J. J.; Mahajan, S. Disentangling the Peak and Background Signals in Surface-Enhanced Raman Scattering. *J. Phys. Chem. C* **2012**, *116*, 6184−6190.
(61) Pavia, D. L.; Lampman, G. M.; Kriz, G. S.; Vyvyan, J. R. *Introduction to Spectroscopy*; CENGAGE: Stamford, 2014.
(62) Kumar, J. S.; Devi, T. R.; Ramkumaar, G.; Bright, A. Ab Initio and Density Functional Theory Calculations of Molecular Structure and Vibrational Spectra of 4-(2-Hydroxyethyl) Piperazine-1-Ethanesulfonic Acid. *Spectrochim. Acta, Part A* **2016**, *152*, 509−522.
(63) Suzuki, S.; Kaneko, S.; Fujii, S.; Marqués-González, S.; Nishino, T.; Kiguchi, M. Effect of the Molecule−Metal Interface on the Surface-Enhanced Raman Scattering of 1,4-Benzenedithiol. *J. Phys. Chem. C* **2016**, *120*, 1038−1042.
(64) Piotrowski, P.; Bukowska, J. Ion Permeation through Silica Coating of Silver Nanoparticles Functionalized with 2-Mercaptoethanesulfonate Anions: Sio_2-Encapsulated SERS Probes for Metal Cations. *J. Phys. Chem. C* **2016**, *120*, 12092−12099.
(65) Kochendoerfer, G. G.; Wang, Z.; Oprian, D. D.; Mathies, R. A. Resonance Raman Examination of the Wavelength Regulation Mechanism in Human Visual Pigments. *Biochemistry* **1997**, *36*, 6577−6587.
(66) Garrell, R. L.; Chadwick, J. E.; Severance, D. L.; McDonald, N. A.; Myles, D. C. Adsorption of Sulfur Containing Molecules on Gold: The Effect of Oxidation on Monolayer Formation and Stability Characterized by Experiments and Theory. *J. Am. Chem. Soc.* **1995**, *117*, 11563−11571.
(67) Socrates, G. *Infrared and Raman Characteristic Group Frequencies: Tables and Charts*, 3 ed.; John Wiley & Sons Ltd.: West Sussex, England, 2001.
(68) Tang, S. Y.; Brown, C. W. Raman Spectra of Gaseous and Matrix-Isolated SO_3. *J. Raman Spectrosc.* **1975**, *3*, 387−390.
(69) Kaldor, A.; Maki, A.; Dorney, A.; Mills, I. The Assignment of N_2 and N_4 of SO_3. *J. Mol. Spectrosc.* **1973**, *45*, 247−252.
(70) Warren, D. S.; McQuillan, A. J. Infrared Spectroscopic and DFT Vibrational Mode Study of Perfluoro (2-Ethoxyethane) Sulfonic Acid (PES), a Model Nafion Side-Chain Molecule. *J. Phys. Chem. B* **2008**, *112*, 10535−10543.
(71) Kudelski, A. Influence of Electrostatically Bound Proteins on the Structure of Linkage Monolayers: Adsorption of Bovine Serum Albumin on Silver and Gold Substrates Coated with Monolayers of 2-Mercaptoethanesulphonate. *Vib. Spectrosc.* **2003**, *33*, 197−204.
(72) Shishlov, N.; Khursan, S. Effect of Ion Interactions on the IR Spectrum of Benzenesulfonate Ion. Restoration of Sulfonate Ion Symmetry in Sodium Benzenesulfonate Dimer. *J. Mol. Struct.* **2016**, *1123*, 360−366.
(73) Lu, G.; Shrestha, B.; Haes, A. J. Importance of Tilt Angles of Adsorbed Aromatic Molecules on Nanoparticle Rattle SERS Substrates. *J. Phys. Chem. C* **2016**, *120*, 20759−20767.
(74) Yang, S.; Dai, X.; Stogin, B. B.; Wong, T.-S. Ultrasensitive Surface-Enhanced Raman Scattering Detection in Common Fluids. *Proc. Natl. Acad. Sci. U. S. A.* **2016**, *113*, 268−273.
(75) Gao, X.; Davies, J. P.; Weaver, M. J. Test of Surface Selection Rules for Surface-Enhanced Raman Scattering: The Orientation of Adsorbed Benzene and Monosubstituted Benzenes on Gold. *J. Phys. Chem.* **1990**, *94*, 6858−6864.
(76) Gao, P.; Weaver, M. J. Surface-Enhanced Raman Spectroscopy as a Probe of Adsorbate-Surface Bonding: Benzene and Monosubstituted Benzenes Adsorbed at Gold Electrodes. *J. Phys. Chem.* **1985**, *89*, 5040−5046.
(77) Yoon, J. H.; Park, J. S.; Yoon, S. Time-Dependent and Symmetry-Selective Charge-Transfer Contribution to SERS in Gold Nanoparticle Aggregates. *Langmuir* **2009**, *25*, 12475−12480.
(78) Wijaya, W.; Pang, S.; Labuza, T. P.; He, L. Rapid Detection of Acetamiprid in Foods Using Surface-Enhanced Raman Spectroscopy (SERS). *J. Food Sci.* **2014**, *79*, T743−T747.
(79) Huber, R. G.; Margreiter, M. A.; Fuchs, J. E.; von Grafenstein, S.; Tautermann, C. S.; Liedl, K. R.; Fox, T. Heteroaromatic Π-Stacking Energy Landscapes. *J. Chem. Inf. Model.* **2014**, *54*, 1371−1379.
(80) Riley, K. E.; Hobza, P. Noncovalent Interactions in Biochemistry. *Wiley Interdiscip. Rev. Comput. Mol. Sci.* **2011**, *1*, 3−17.

DOI: 10.1021/jacs.8b13211
J. Am. Chem. Soc. 2019, 141, 4034−4042